Article | Open Access

Energy Materials

Mao *et al. Energy Mater.* **2026**, *6*, 600130 **DOI:**10.20517/energymater.2026.153

Corrosion-induced surface reconstruction enhances RuO_2/NiFe(OH)$_x$ for efficient hydrogen evolution reaction

Chenxing Mao[1,#], Chang Zhang[2,#], Jie Chen[3], Junpo Guo[3,*], Zhifei Cui[1], Rongtao Zhang[1], Xin Li[1], Rui Li[4], Yinan Liu[4,*], Xupo Liu[1,3,*]

Keywords:
Hydrogen evolution reaction, water splitting, NiFe hydroxides, surface reconstruction, corrosion strategy

Citation: Mao, C.; Zhang, C.; Chen, J.; Guo, J.; Cui, Z.; Zhang, R.; Li, X.; Li, R.; Liu, Y.; Liu, X. Corrosion-induced surface reconstruction enhances RuO_2/NiFe(OH)$_x$ for efficient hydrogen evolution reaction. *Energy Mater.* **2026**, *6*, 600130. https://dx.doi.org/10.20517/energymater.2026.153

Received: 3 Jun 2026
First Decision: 25 Jun 2026
Revised: 4 Aug 2026
Accepted: 18 Aug 2026
Published: 29 Sep 2026

Academic Editor:
Hong Li
Copy Editor:
Ping Zhang
Production Editor:
Ping Zhang

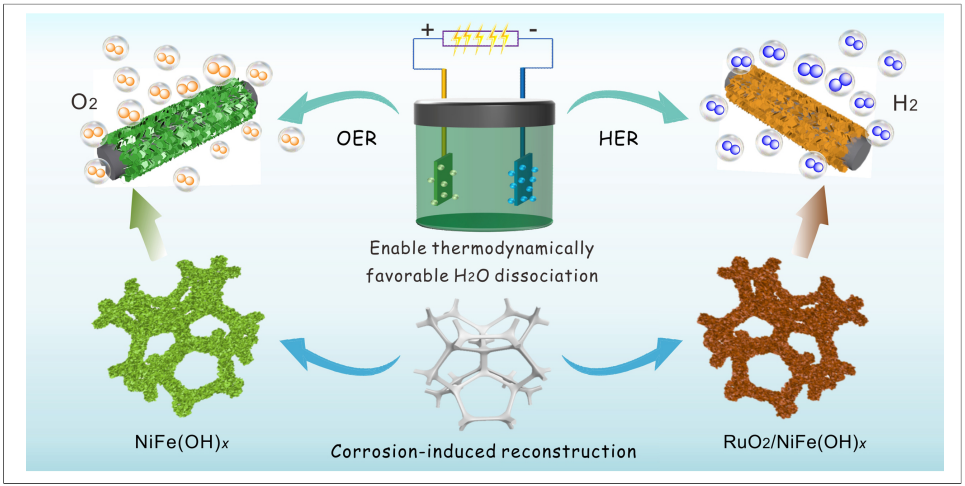

Abstract

NiFe hydroxide has emerged as a highly promising electrocatalyst in water electrolysis, yet its application in catalyzing the hydrogen evolution reaction (HER) remains challenging. Herein, we report a corrosion-reconstruction strategy to fabricate RuO_2 nanocluster-endowed NiFe hydroxide [RuO_2/NiFe(OH)$_x$] as an efficient electrocatalyst for HER application. Density functional theory (DFT) calculations provide insight into the HER mechanism, revealing that the reconstructed surface enriched with RuO_2 nanoclusters optimally adsorbs water molecules. This modification also induces a shift of the *H adsorption site from oxygen atoms to ruthenium atoms due to electron transfer effects, facilitating the desorption of *H and promoting efficient H_2 formation. The synthesized RuO_2/NiFe(OH)$_x$ catalyst delivers prominent HER activity (149 mV at 100 mA cm^{-2}) and robust operational stability in a water-splitting device, sustaining 200 mA cm^{-2} for 100 h

[1]Henan Engineering Research Center of Design and Recycle for Advanced Electrochemical Energy Storage Materials, School of Materials Science and Engineering, Henan Normal University, Xinxiang 453007, Henan, China.
[2]School of Materials Science and Engineering, Huazhong University of Science and Technology, Wuhan 430074, Hubei, China.
[3]School of Chemistry and Chemical Engineering, Henan Normal University, Xinxiang 453007, Henan, China.
[4]Joint Key Laboratory of the Ministry of Education, Institute of Applied Physics and Materials Engineering, University of Macau, Macao 999078, China.
[#]These authors contributed equally to this work.

***Correspondence to:** Dr. Junpo Guo, School of Chemistry and Chemical Engineering, Henan Normal University, Xinxiang 453007, Henan, China. E-mail: guojunpo@htu.edu.cn; Dr. Yinan Liu, Joint Key Laboratory of the Ministry of Education, Institute of Applied Physics and Materials Engineering, University of Macau, Macao 999078, China. E-mail: yc27809@um.edu.mo; Prof. Xupo Liu, Henan Engineering Research Center of Design and Recycle for Advanced Electrochemical Energy Storage Materials, School of Materials Science and

Engineering, Henan Normal University, Xinxiang 453007, Henan, China. E-mail: liuxupo@htu.edu.cn

with almost no obvious voltage increment. Importantly, the fabrication of a large-area electrode demonstrates that this simple, room-temperature corrosion-reconstruction strategy is a promising and viable route for the application of HER electrocatalysts.

INTRODUCTION

The increasingly flourishing hydrogen energy economy promotes the rapid development of water splitting to fabricate high-purity hydrogen[1,2]. Water splitting can be conducted by employing the electrical energy produced by solar and wind energy, which has the obvious advantages of cleanliness, no pollution and high sustainability[3,4]. However, the recent progress of water splitting has been severely hindered by the high cost of electrocatalysts. Nowadays, the widely used hydrogen evolution reaction (HER) electrocatalysts are focused on Pt-based precious metal catalysts, bringing forth the high cost for water splitting[5-9]. Developing low-cost electrocatalysts to replace Pt-based catalysts has been widely recognized goal, which has attracted considerable attention from researchers[10-12].

Among the various kinds of investigated HER catalysts, phosphides, sulfides, carbides and nitrides have been studied by many groups owing to their excellent HER activity[13-18]. However, these catalysts are generally synthesized through the high-temperature calcination or the hydrothermal treatment[19-23]. The complex steps and huge energy consumption increase the production cost of HER catalysts. Therefore, searching for simpler and more available methods of catalyst preparation is urgent for water splitting. Corrosion engineering is a recently developed strategy for achieving electrocatalysts relying on the formed corrosion layers on metal substrates as electrochemical active layers[24-28]. In general, metal corrosion can spontaneously occur in a high-humidity environment at room temperature. The corrosion layers are always composed of hydroxides, which are also applied as electrocatalytic materials[29-31]. Based on this recognition, metal corrosion is applied for preparing highly active electrocatalysts with the aim of "turning damage into treasure". Previous works on corrosion engineering mainly focus on oxygen evolution reaction (OER) catalysts, while the investigations of HER catalysts are still very few. The main problem of HER catalysts based on metal corrosion is the poor HER activity of the hydroxide corrosion layers due to the strong *H adsorption[32]. Thus, employing an effective strategy to modulate the electronic structures of corrosion layers is necessary to enhance the HER performance[33]. RuO_2 was thereby selected as the targeted modifier, based on its well-documented near-optimal ΔG_{H^*} value close to 0 eV that can precisely compensate for the sluggish hydrogen desorption kinetics of the hydroxide layer[34]. While some prior works have adopted corrosion engineering to fabricate RuO_2-modified hydroxide catalysts for boosted HER performance, the dynamic surface structural reconstruction process of the catalyst before and after RuO_2 modification has not been investigated.

Towards simplifying the synthesis procedures of HER catalysts, we proposed a facile corrosion-reconstruction strategy in this work to fabricate the RuO_2/NiFe(OH)$_x$ HER electrocatalysts at room temperature. Actually, the cleaned NiFe foams (NFF) were immersed in the $NiCl_2$ solution for 9 h to obtain the NiFe hydroxide [NiFe(OH)$_x$]. In the subsequent step, the prepared catalyst was immersed in a 2 mM $RuCl_3$ solution for 2 h to achieve surface reconstruction, and the resulting sample was labeled as RuO_2/NiFe(OH)$_x$. The as-synthesized electrocatalysts display ultrahigh HER activity, achieving current densities of 50 mA cm^{-2} and 100 mA cm^{-2} recorded at the low overpotentials of merely 111 mV and 149 mV. Moreover, the assembled water-splitting device could stably run under the relevant large current density of 200 mA cm^{-2} lasting for 100 h. Density functional theory (DFT) calculations reveal that the reconstructed surface enriched with RuO_2 nanoclusters optimally adsorbs water molecules and induces a shift in *H

adsorption from oxygen to ruthenium atoms, facilitating the desorption of *H and promoting efficient H_2 formation. This work supplies a facile method of preparing efficient HER catalysts at room temperature, largely simplifying the synthesis of HER electrocatalysts. We believe the simple corrosion strategy can effectively boost the practical application of HER catalysts for water splitting.

EXPERIMENTAL

Materials

The NFF used was purchased from Kunshan Tengerhui Electronic Technology Co., Ltd. $NiCl_2·6H_2O$ and $RuCl_3·xH_2O$ were bought from Aladdin Chemical Reagents Co., Ltd. Absolute ethanol was supplied by Sinopharm Chemical Reagent Co., Ltd. Fe foam, Ni foam, Cu foam and stainless steel mesh were bought from Suzhou Taiter Metallic Foam Co., Ltd. Deionized water was employed to wash samples and prepare reaction solutions. The instruments used for catalyst preparation, structural characterization and performance testing are listed in Supplementary Table 1.

Fabrication of RuO_2/NiFe(OH)$_x$ electrocatalysts

RuO_2/NiFe(OH)$_x$ electrocatalysts were prepared through a corrosion-reconstruction strategy. First, the NFF (2 × 2 cm^2) was sequentially washed with ethanol, 1 M HCl solution, and water three times by ultrasonication. The cleaned NFF was soaked in the 100 mM $NiCl_2$ solution for 9 h to complete the first corrosion and the obtained sample was denoted as NiFe(OH)$_x$. Next, the pre-synthesized catalyst was immersed in a 2 mM $RuCl_3$ solution (theoretical concentration) for 2 h to achieve the second corrosion. To guarantee the homogeneous deposition of corrosion layers on both sides of the NFF, magnetic stirring was applied in the whole reaction process at a stirring speed of 100 rpm. Then, the NFF was washed repeatedly using deionized water and ethanol to eliminate residual surface contaminants. After drying under vacuum for 12 h, the final sample of RuO_2/NiFe(OH)$_x$ was obtained.

To explore the universality of the corrosion-reconstruction strategy, the other four catalysts were also synthesized by using iron foam (IF), Ni foam (NF), Cu foam (CF) and stainless steel mesh (SSM) as substrates (size: 2 × 2 cm^2), which were named as C-IF, C-NF, C-CF and C-SSM, respectively. Moreover, taking a piece of NFF (8 × 8 cm^2) as substrate, a large-size RuO_2/NiFe(OH)$_x$ electrocatalyst was fabricated through a similar method.

Physical characterization

The morphological characterization of the corrosion-derived active layers was performed using a FEI Sirion200 Field Emission Scanning Electron Microscope (SEM). All transmission electron microscopy (TEM) imaging was carried out on a ThermoFisher Scientific Talos F200X transmission electron microscope (the acceleration voltage was set to 200 kV). This instrument is equipped with a Gatan Enfina electron spectrometer for electron energy loss spectroscopy (EELS) elemental mapping analysis. The crystalline phases of the fabricated catalysts were examined via X-ray diffraction (XRD) on an X'Pert^3 Powder diffractometer using Cu-Kα radiation. The surface element compositions and chemical valences of catalysts were detected through an ESCALAB 250Xi X-ray photoelectron spectroscopy (XPS).

Electrochemical characterization

A CHI660E electrochemical workstation (Chenhua) was used for the electrochemical test. Firstly, the corrosion polarization curves of the cleaned NFF and NiFe(OH)$_x$ electrodes were tested. The three-electrode testing system was assembled using the as-fabricated working electrode, a graphite rod, and a saturated calomel electrode (SCE). The stable value of open-circuit voltage (OCV) was obtained after operating for 400 s, and then the linear sweep voltammetry (LSV) curve was measured within the range of OCV ± 300 mV (the scanning rate was set to 1 mV s^{-1}). The HER electrocatalytic property was subsequently evaluated in a

classic three-electrode system by employing the prepared catalyst, a graphite rod counter electrode and an Hg/HgO reference electrode. The working electrode was cut into 0.5 × 1 cm^2 pieces, fixed on the electrode holder, and measured with a 0.25 cm^2 effective reaction area. The LSV curves were recorded over the potential window from 0 V to -0.4 V in the N_2-saturated 1.0 M KOH electrolyte. The Nyquist plots at -0.05 V were determined to obtain the impedance values of the working electrodes in the frequency range covering 0.01-0.1 MHz. Electrochemically active surface area (ECSA) were estimated by testing the cyclic voltammetry (CV) curves in 0.1-0.3 V under different sweep rates ranging from 20 to 100 mV s^{-1} (interval of 20 mV s^{-1}). The durability test was conducted at a current density of 200 mA cm^{-2} for 100 h through the chronopotentiometry method. The overall water-splitting electrolyzer was constructed by using the RuO_2/$NiFe(OH)_x$ electrode as the cathode and the $NiFe(OH)_x$ electrode as the anode. The stability of the water-splitting device was evaluated through the chronopotentiometry method under the current densities maintained at 100 mA cm^{-2} and 200 mA cm^{-2} for 100 h. All the electrochemical data presented in this manuscript have not undergone iR compensation.

Theoretical calculation

The Vienna Ab initio Simulation Package (VASP) was utilized to optimize the structure of FeNiOOH and FeNiOOH modified with RuO_2 (RuO_2/FeNiOOH). The exchange-correlation potential was treated within the generalized gradient approximation (GGA) framework, in which the revised Perdew-Burke-Ernzerhof (RPBE) formalism was adopted. The cutoff energy was set to 500 eV to expand the wave function. A Γ-point-centered 1 × 1 × 1 k-point mesh was adopted for surface calculations. The applied force and energy tolerance were separately defined as 0.05 eV $Å^{-1}$ and 10^{-5} eV. The free energy pathway of HER on different sites was calculated by applying the computational hydrogen electrode (CHE) model[35], and this can be converted to the adsorption free energy by adding zero-point energy (ZPE) and entropy (TS) as given in:

$$\Delta G = \Delta E + \Delta ZPE - T\Delta S \quad (1)$$

RESULTS AND DISCUSSION

A RuO_2/$NiFe(OH)_x$ electrode was synthesized via a facile corrosion-reconstruction strategy for HER applications, as illustrated in Figure 1A. Initially, a cleaned NFF was immersed in a $NiCl_2$ solution to facilitate the formation of $NiFe(OH)_x$ layers. Afterward, the already synthesized $NiFe(OH)_x$ catalyst was introduced into a $RuCl_3$ solution, leading to the generation of RuO_2 nanoclusters that were strategically decorated on the $NiFe(OH)_x$ surface. These decorated RuO_2 clusters serve to modulate the electronic configuration of $NiFe(OH)_x$, thereby enabling highly efficient hydrogen evolution performance.

A preliminary investigation into the corrosion behaviors of $NiFe(OH)_x$ and NFF was conducted to explore the preparation process of electrodes. The optical images of the synthesized NFF, $NiFe(OH)_x$, and RuO_2/$NiFe(OH)_x$ electrodes are displayed in the inset of Figure 1B and C. The distinct yellow color of $NiFe(OH)_x$ and the black appearance of RuO_2/$NiFe(OH)_x$ starkly contrast with the pristine silver color of NFF, signifying a corrosion-induced transformation in the composition and structure of NFF. By fitting the corrosion polarization curves depicted in Figure 1B and C, it is observed that the corrosion current density of NFF in a $NiCl_2$ solution (0.551 mA cm^{-2}) significantly exceeded that in water (0.045 mA cm^{-2}). Concurrently, the corrosion potential of NFF in the $NiCl_2$ solution (-0.635 V) was lower than that in water (-0.454 V). Analogously, $NiFe(OH)_x$ delivered a higher corrosion current density (0.367 mA cm^{-2}) and a lower corrosion potential (-0.509 V) in a $RuCl_3$ solution compared to those in water (0.005 mA cm^{-2} and -0.439 V, respectively) [Figure 1D]. These findings underscore the accelerated corrosion rates in $NiCl_2$ and $RuCl_3$ solutions, attributable to the potent corrosivity of Cl^- ions and the enhanced ionic conductivity of metal salt solutions. Furthermore, the corrosion current density of $NiFe(OH)_x$ in water (0.005 mA cm^{-2}) was notably

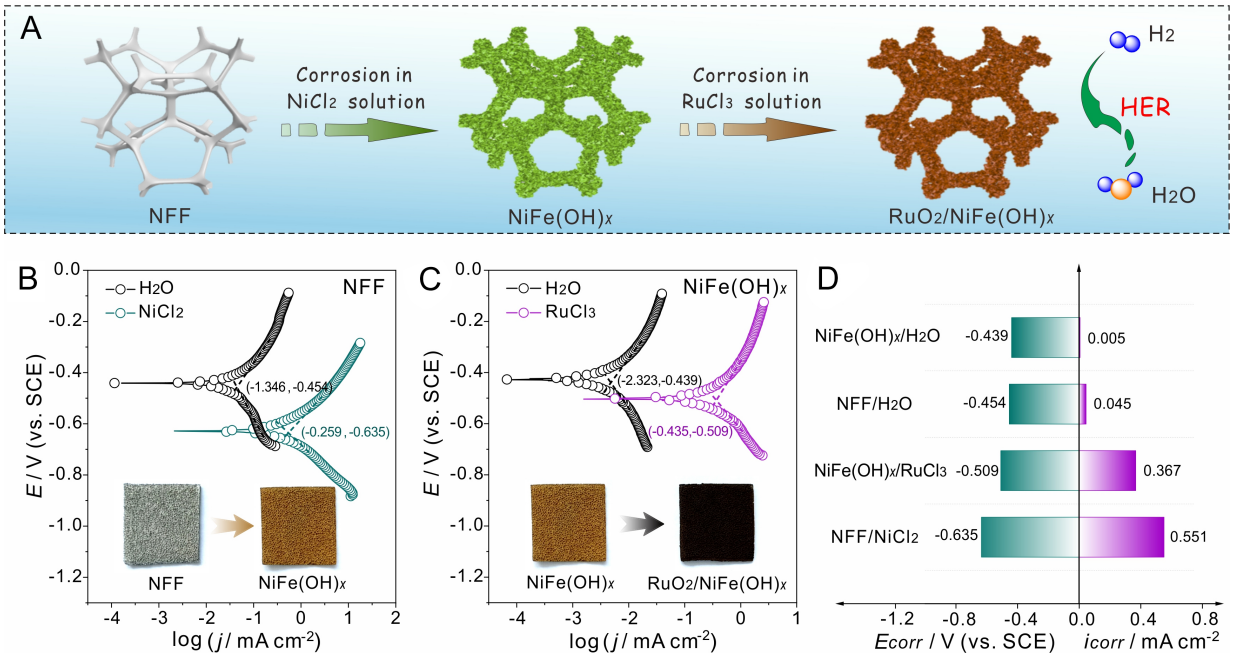

Figure 1. (A) Corrosion-derived surface reconstruction of NFF for achieving efficient RuO_2/NiFe(OH)$_x$ electrocatalysts; (B and C) Corrosion polarization curves (inset: photos of the synthesized NFF, NiFe(OH)$_x$ and RuO_2/NiFe(OH)$_x$ electrodes); (D) Comparison of the calculated corrosion potentials and corrosion current densities. NFF: NiFe foams; SCE: saturated calomel electrode; HER: hydrogen evolution reaction.

lower than that of NFF (0.045 mA cm^{-2}), which can be ascribed to the protective NiFe(OH)$_x$ layers grown on the NFF surface, impeding further corrosion of the NFF substrate by the aqueous medium. Consequently, by modulating the corrosion behavior of metals, it becomes feasible to engineer surface structural reconstructions in catalysts, thereby optimizing their performance for HER applications.

SEM images were used to investigate the surface morphologies of catalysts. As displayed in Supplementary Figure 1, the pristine NFF displays a smooth surface without any grown materials. After the first corrosion in $NiCl_2$ solution, uniform flower-like nanosheet arrays were generated over the surface of NiFe(OH)$_x$. Then, the second corrosion in $RuCl_3$ solution did not change the nanosheet morphology of the RuO_2/NiFe(OH)$_x$ electrode [Supplementary Figure 2]. Moreover, the TEM images were also used to reveal the structure of RuO_2/NiFe(OH)$_x$. It is notable that the corrosion layers of RuO_2/NiFe(OH)$_x$ consist of many thin nanosheets [Figure 2A and B], which are beneficial for promoting the exposure of electrochemically active sites. The TEM image shown in Figure 2C indicates the lattice fringes of corrosion layers, in which the lattice fringes with a spacing of 0.626 nm are associated with the (020) plane of FeOOH (JCPDS 73-2326). It is also observed that there are some nanoclusters on the nanosheets, which contain lattice fringes with a spacing of 0.255 nm and 0.315 nm belonging to the (101) and (110) crystalline planes of RuO_2 (JCPDS 88-0323)[36]. The elemental mapping images presented in Figure 2D-G reveal the uniform elemental dispersion of Ni, Fe, Ru, and O within the nanosheet arrays, confirming the successful loading of Ru species on the NiFe(OH)$_x$ nanosheets. In addition, XRD patterns of the catalysts were recorded to analyze phase composition. As depicted in Supplementary Figure 3, no obvious diffraction peaks were observed except the peaks of NFF substrates ($FeNi_3$: PDF#38-0419)[37], demonstrating the low crystallinity of corrosion layers. The above-mentioned results prove that the corrosion layers of the RuO_2/NiFe(OH)$_x$ electrode are composed of the RuO_2 nanoclusters-decorated NiFe(OH)$_x$ nanosheet arrays.

The surface compositions and valence states of these catalysts were investigated through the XPS spectra. The survey XPS spectra in Supplementary Figure 4 prove the co-presence of Fe, Ni and O elements for the

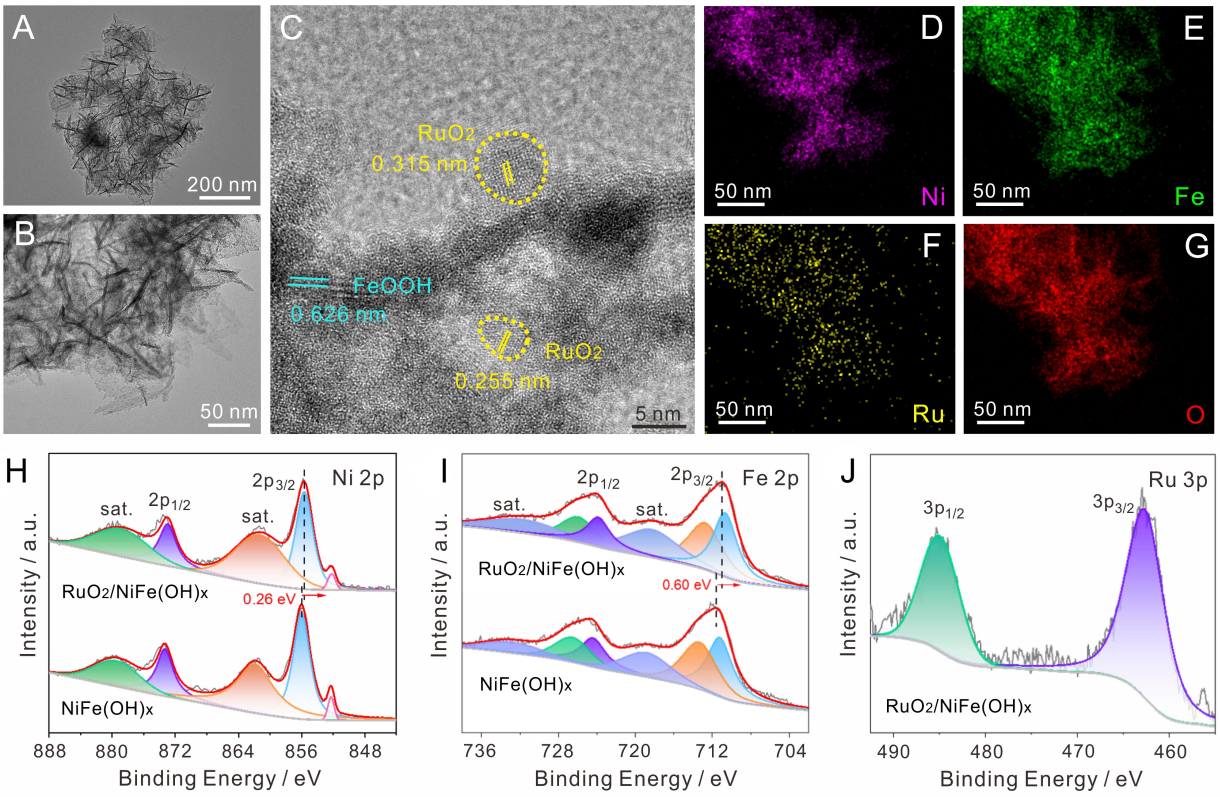

Figure 2. (A and B) TEM images of $RuO_2/NiFe(OH)_x$; (C) High-resolution TEM image of $RuO_2/NiFe(OH)_x$; (D-G) Elemental mapping images of $RuO_2/NiFe(OH)_x$; (H-J) XPS spectra for Ni 2p regions, Fe 2p regions and Ru 3p regions. TEM: Transmission electron microscopy; XPS: X-ray photoelectron spectroscopy.

$NiFe(OH)_x$ and $RuO_2/NiFe(OH)_x$ samples. It is noteworthy that the Ru elements are detected in $RuO_2/NiFe(OH)_x$, revealing the available loading of Ru on active layers. Ni 2p spectrum of $RuO_2/NiFe(OH)_x$ in Figure 2H is divided into five peaks. The binding energies located at 855.64 eV and 872.96 eV are attributed to the Ni 2p3/2 and Ni 2p1/2 peaks as well as two satellite peaks centered at 861.58 eV and 879.45 eV, revealing the generation of Ni^{2+} species in the $RuO_2/NiFe(OH)_x$[38,39]. Besides, the Ni^0 peak is observed at 852.19 eV, which is caused by the NFF substrates. Figure 2I depicts the Fe 2p XPS spectrum of $RuO_2/NiFe(OH)_x$, in which the binding energies centered at 710.69 eV and 723.91 eV are assigned to the Fe^{2+} ions, and the binding energies of 712.89 eV and 726.15 eV belong to the Fe^{3+} ions[33,40]. The Fe 2p XPS spectrum indicates the co-presence of Fe^{2+}/Fe^{3+} species in $RuO_2/NiFe(OH)_x$. Three O species are detected for $RuO_2/NiFe(OH)_x$ at 529.73, 531.19, and 532.18 eV in O 1s spectrum [Supplementary Figure 5], which correspond to the M-O, M-OH and H_2O bonds, respectively[41,42]. For the Ru 3p spectrum [Figure 2J], the binding energies at 462.81 eV and 485.10 eV are ascribed to the Ru^{4+} ions, further confirming the RuO_2 clusters in the active layers of $RuO_2/NiFe(OH)_x$[43]. Moreover, the binding energies of Fe 2p3/2, Ni 2p3/2 and O 1s for $RuO_2/NiFe(OH)_x$ all shift negatively toward lower binding energy in contrast with those of $NiFe(OH)_x$. In general, this reveals the existence of electron transfer between the RuO_2 cluster and $NiFe(OH)_x$ nanosheets, along with local electron rearrangement on the surface of $NiFe(OH)_x$ induced by RuO_2 nanoclusters.

To clarify the formation mechanism of $RuO_2/NiFe(OH)_x$, we have provided the time-dependent color evolution and pH change of $RuCl_3$ solution, and Inductively coupled plasma optical emission spectrometry (ICP-OES) analysis of Ru, Ni, and Fe concentrations before and after immersion. During the immersion process, the initial orange color of $RuCl_3$ solution gradually turned blue [Supplementary Figure 6]. Usually,

the Ru^{3+} solution appears yellow, while the Ru^{2+} solution appears blue. The above color change indicates that a redox reaction has occurred between Ru^{3+} ions and NiFe-substrate of the $NiFe(OH)_x$ catalyst. At longer immersion times, the solution became darker and slightly turbid, which is attributed to the slight detachment of newly formed $RuO_2/NiFe(OH)_x$ corrosion layers. Meanwhile, the pH value increased from 3.10 to 5.00 [Supplementary Table 2], resulting from the consumption of Ru^{3+} ions and partial dissolution of surface Ni/Fe-hydroxide species. ICP results in Supplementary Table 3 show that the Ni and Fe concentrations increase markedly from 0.0949 and 0.3047 mg L^{-1} to 68.1262 and 210.2132 mg L^{-1} after 2 h immersion, verifying the dissolution and reconstruction of $NiFe(OH)_x$ in the acidic $RuCl_3$ solution. The Ru concentration decreases from 145.7364 mg L^{-1} (1.44 mM) to 19.9406 mg L^{-1}, indicating the consumption and deposition of Ru species on the electrode surface. Considering the solution volume of 30 mL and the electrode area of 4 cm^2, the calculated Ru loading on $RuO_2/NiFe(OH)x$ was 0.94 mg cm^{-2}. Thus, it can be concluded that the redox reaction between Ru^{3+} ions and the NiFe substrate is the main reason for the corrosion-induced reconstruction of $NiFe(OH)_x$ in $RuCl_3$ solution. The reduced Ru species are unstable and are further oxidized to form the RuO_2 phase, resulting in the construction of $RuO_2/NiFe(OH)_x$ corrosion layers.

The electrochemical hydrogen evolution reaction (HER) performances of the NFF, $NiFe(OH)_x$, and $RuO_2/NiFe(OH)_x$ electrocatalysts were meticulously evaluated in 1 M KOH electrolyte. As evident from the polarization curves presented in Figure 3A, both the pristine NFF and $NiFe(OH)_x$ electrodes exhibit markedly poor HER activity. However, a notable enhancement in the HER activity of $NiFe(OH)_x$ is observed subsequent to its surface reconstruction via corrosion in a $RuCl_3$ solution. Notably, the $RuO_2/NiFe(OH)_x$ sample achieves remarkable HER performance, demanding a small overpotential of merely 111 mV to attain a current density of 50 mA cm^{-2} [Figure 3B]. This HER performance outperforms that of both NFF (350 mV) and $NiFe(OH)_x$ (276 mV) by a significant margin. We have supplemented the benchmark comparison with commercial Pt/C (20 wt%), as shown in Supplementary Figure 7. The $RuO_2/NiFe(OH)_x$ shows a slightly lower current density than Pt/C at low overpotentials, but significantly outperforms it at high overpotentials, highlighting its prominent advantages. The exceptional HER activity demonstrated by $RuO_2/NiFe(OH)_x$ is primarily ascribed to the electronic interplay between RuO_2 nanoclusters and $NiFe(OH)_x$, along with the augmented exposure of electrochemically active sites facilitated by the nanosheet arrays.

Besides, the corresponding Tafel slopes were calculated to evaluate the HER mechanism [Figure 3C]. It is found that the Tafel slope of $RuO_2/NiFe(OH)_x$ is 33.70 mV dec^{-1}, much smaller than those of NFF (261.05 mV dec^{-1}) and $NiFe(OH)_x$ (183.01 mV dec^{-1}), revealing a faster HER process. Furthermore, the Nyquist curves of NFF, $NiFe(OH)_x$ and $RuO_2/NiFe(OH)_x$ were also tested to study the charge-transfer resistance (R_{ct}) [Figure 3D]. It is clearly observed that $RuO_2/NiFe(OH)_x$ displays the lowest R_{ct} value among these catalysts, indicating quick electron transfer in the electrochemically process. Generally, the C_{dl} values can be adopted to quantify the ECSA of electrocatalysts. The C_{dl} values of NFF, $NiFe(OH)_x$ and $RuO_2/NiFe(OH)_x$ were calculated from the CV curves in Supplementary Figure 8. It can be seen from Figure 3E that $RuO_2/NiFe(OH)_x$ contains the highest C_{dl} of 227.66 mF cm^{-2} among the three catalysts. We calculated the ECSA using the obtained C_{dl} values in Figure 3E according to the equation ($ECSA = A_{geo}*C_{dl}/C_s$, C_s = 40 μF cm^{-2}, A_{geo} refers to the effective reaction area). The calculated ECSA values for NFF, $NiFe(OH)_x$ and $RuO_2/NiFe(OH)_x$ are 303.63, 426.44 and 1,422.88 cm^2, respectively. We have also provided the ECSA-normalized HER polarization curves. As shown in Supplementary Figure 9, $RuO_2/NiFe(OH)_x$ still exhibits superior HER activity after ECSA normalization compared with $NiFe(OH)_x$ and NFF. The obtained result verifies that the improved HER performance is not solely caused by the enlarged surface area, but also originates from the enhanced intrinsic activity of $RuO_2/NiFe(OH)_x$.

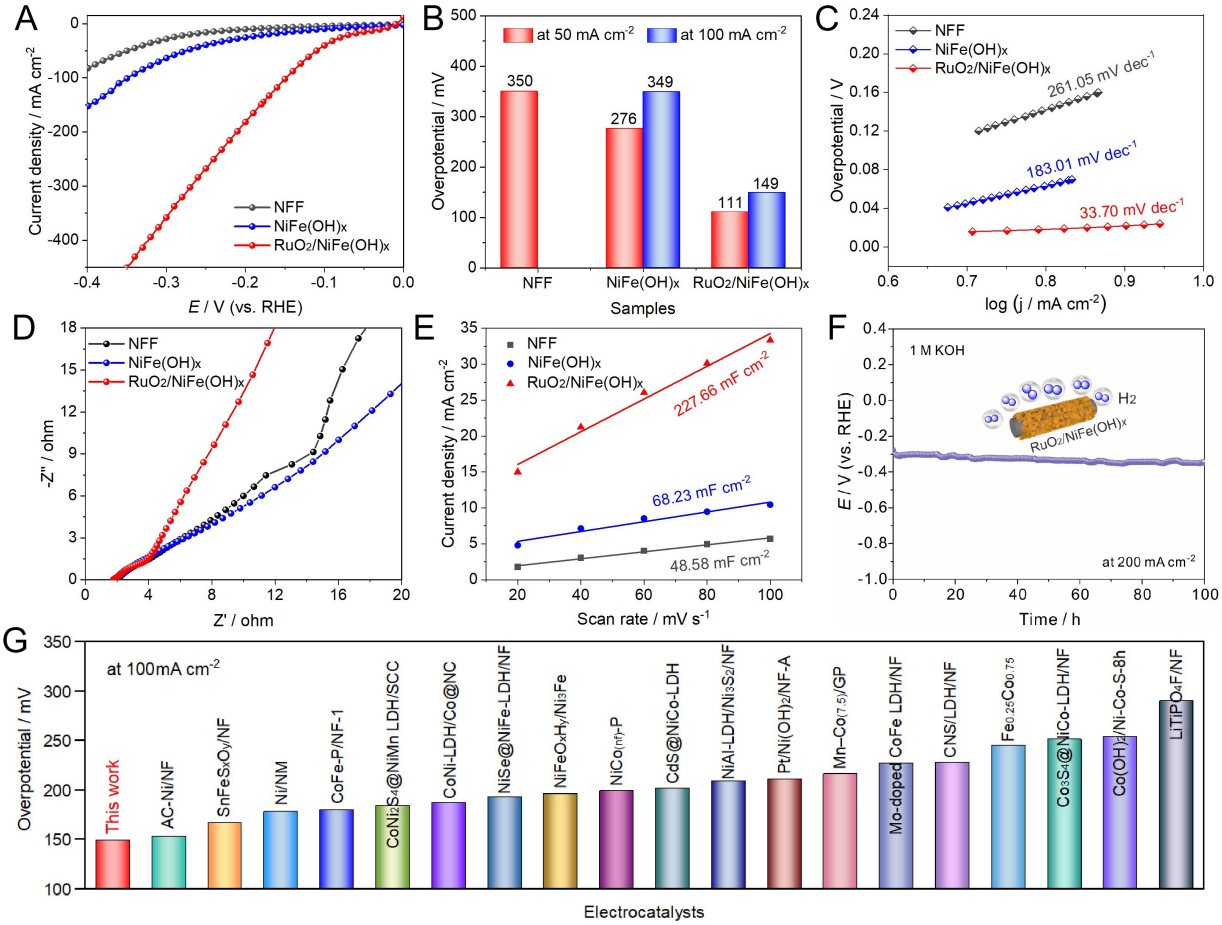

Figure 3. (A) Polarization curves of NFF, NiFe(OH)$_x$ and RuO$_2$/NiFe(OH)$_x$ electrocatalysts; (B) A comparison of the required overpotentials measured at 50 mA cm^{-2} and 100 mA cm^{-2} current densities; (C) The associated Tafel slopes; (D) Nyquist curves; (E) Linear changes of current densities versus the scanning rates; (F) Chronopotentiometry curve of RuO$_2$/NiFe(OH)$_x$ at the constant current density of 200 mA cm^{-2} for 100 h. (G) Comparison of the overpotential of RuO$_2$/NiFe(OH)$_x$ at 100 mA cm^{-2} with the recently published HER electrocatalysts. NFF: NiFe foams; HER: hydrogen evolution reaction; RHE: reversible hydrogen electrode.

Furthermore, the operating stability of RuO$_2$/NiFe(OH)$_x$ was detected through the chronopotentiometry method. The RuO$_2$/NiFe(OH)$_x$ displays slight changes in applied potentials after operation at 200 mA cm^{-2} for 100 h [Figure 3F], demonstrating admirable durability. For catalysts fabricated via corrosion engineering, the coupling between corrosion layers and substrates has non-negligible weaknesses: partial exfoliation of corrosion layers occurs under high-current operation. Thus, moderately reducing the corrosion rate during preparation facilitates homogeneous and steady growth of corrosion layers, which can improve the interfacial adhesion stability of catalysts. Moreover, the HER activity of RuO$_2$/NiFe(OH)$_x$ is compared with recently reported electrocatalysts, as shown in Figure 3G and Supplementary Table 4. It is noteworthy that the overpotential of RuO$_2$/NiFe(OH)$_x$ at 100 mA cm^{-2} is much lower than that of most of the reported catalysts. Thus, it can be inferred that the synthesized RuO$_2$/NiFe(OH)$_x$ possesses excellent HER activity and durability. SEM images of RuO$_2$/NiFe(OH)$_x$ after the durability determination reveal substantial reconstruction of the nanosheet architecture, evidenced by the formation of abundant nanoparticles across the surface [Supplementary Figure 10]. XPS spectra in Supplementary Figure 11 verify that distinct Ru species are clearly preserved on the catalyst following prolonged electrolysis. The robust electronic coupling between these residual Ru species and Ni/Fe active sites imparts the catalyst with prominent electrocatalytic activity and exceptional long-term operational stability. To verify the hydrogen generation efficiency, the measurement of Faradaic efficiency for RuO$_2$/NiFe(OH)$_x$ was conducted using the water-displacement

method [Supplementary Figure 12]. The measured amount of H_2 evolution was similar to the theoretical value calculated from Faraday's law, corresponding to a Faradaic efficiency of 87.5%. This confirms that the RuO_2/NiFe(OH)$_x$ catalyst enables efficient H_2 generation during HER.

To gain a deeper insight into the HER mechanism on RuO_2/NiFe(OH)$_x$ surfaces, we performed a comprehensive mechanistic analysis employing DFT calculations. FeNiOOH was adopted as an idealized model to describe the local coordination environment of the experimentally prepared NiFe(OH)$_x$ catalyst. This model aims to capture the essential interfacial electronic interactions with RuO_2 under HER operating conditions. The differential charge density depicted in Figure 4A, and Bader charge analysis in Supplementary Figures 13-15 and Supplementary Tables 5-7 provide compelling evidence of electron redistribution within FeNiOOH, induced by the incorporation of a RuO_2 nanocluster. These results reveal that RuO_2 donates electrons to NiFe(OH)$_x$, leading to electron enrichment of the NiFe(OH)$_x$ side and local interfacial charge polarization. Figure 4B shows the calculated reaction free energy changes for the water dissociation-related process on FeNiOOH and RuO_2/FeNiOOH. The pristine FeNiOOH surface exhibits a strong interaction with water-derived intermediates, corresponding to a largely negative reaction free energy change of -0.7206 eV. After the introduction of RuO_2 nanoclusters, this value is moderated to -0.0125 eV, indicating that RuO_2 modulates the thermodynamic favorability of water adsorption and dissociation on FeNiOOH. Furthermore, the introduction of RuO_2 nanoclusters leads to an optimization of the adsorption free energy for hydrogen atoms, as illustrated in Figure 4C. Figure 4D presents the optimized and established water dissociation models on both the FeNiOOH and RuO_2/FeNiOOH surfaces. On the FeNiOOH surface, the preferred adsorption site for the hydrogen intermediate (*H) is located at the oxygen atom, resulting in a robust adsorption interaction that hinders the desorption of *H and subsequent H_2 formation. However, upon the incorporation of RuO_2 nanoclusters, the adsorption site of *H shifts to the ruthenium atom due to the electron transfer effect. This shift is accompanied by a change in the adsorption free energy from -1.7966 eV to 0.5112 eV [Figure 4C], facilitating the desorption of *H and H_2 evolution. The DFT calculations offer robust evidence that the electronic interaction mechanism between RuO_2 nanoclusters and FeNiOOH significantly enhances the HER property of the RuO_2/NiFe(OH)$_x$ catalyst under alkaline conditions.

The overall water-splitting device was constructed to explore the potential applicability of RuO_2/NiFe(OH)$_x$, as depicted in Figure 5A. The as-prepared NiFe(OH)$_x$ catalyst serves as the anodic electrode, and its OER performance has also been evaluated. The LSV curves and a comparison of overpotentials presented in Figure 5B and C reveal that NiFe(OH)$_x$ can achieve the current densities of 50 mA cm^{-2} and 100 mA cm^{-2} by supplying the small overpotentials of 196 mV and 257 mV, respectively, much smaller than those of NFF (290 mV and 325 mV). The enhanced OER activity is ascribed to the generation of NiFe(OH)$_x$ corrosion layers on the NFF substrate. For comparison, a water-splitting device utilizing NFF‖NFF has also been assembled. As evident from the polarization curves in Figure 5D, the NiFe(OH)$_x$‖RuO_2/NiFe(OH)$_x$-based water-splitting device exhibits superior performance compared to the NFF‖NFF device. Notably, to attain a current density of 50 mA cm^{-2}, the constructed NiFe(OH)$_x$‖RuO_2/NiFe(OH)$_x$ device requires a voltage of merely 1.556 V, considerably lower than the 1.909 V demanded by the NFF‖NFF electrolyzer. Moreover, to assess the practical application potential, the durability of the water electrocatalysis device is evaluated. As depicted in Figure 5E, the chronopotentiometry curves of the NiFe(OH)$_x$‖RuO_2/NiFe(OH)$_x$ device show remarkable operational stability, maintaining stable performance even at high current densities of 100 mA cm^{-2} and 200 mA cm^{-2} with only a slight increase in potential after the 100 h testing. Furthermore, a comparative analysis of the water-splitting performance of the NiFe(OH)$_x$‖RuO_2/NiFe(OH)$_x$ system with recently reported devices, as summarized in Supplementary Table 8, confirms that both the NiFe(OH)$_x$ and RuO_2/NiFe(OH)$_x$ possess outstanding durability, making them promising candidates for practical water-splitting applications.

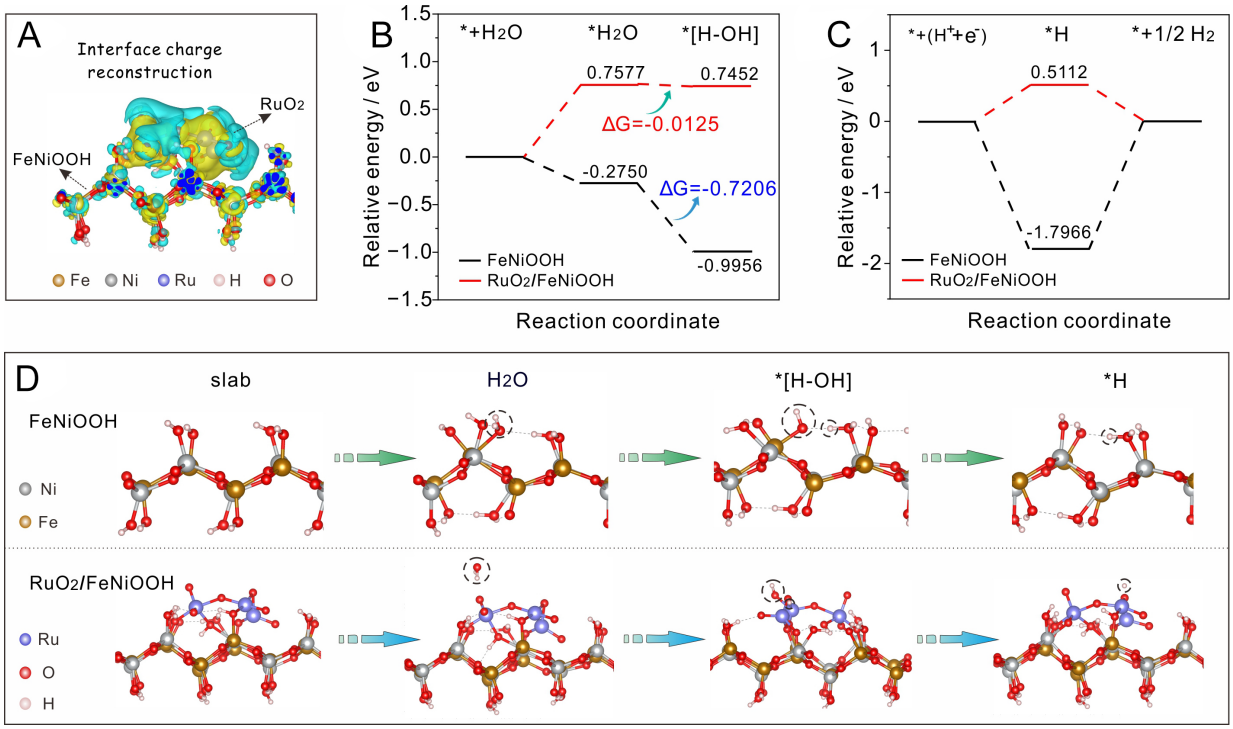

Figure 4. (A) The differential charge density for RuO_2/FeNiOOH (the isosurface is set to 0.005 e $Bohr^{-3}$. The yellow region corresponds to electron accumulation, while the cyan region denotes electron depletion); The reaction free energies of (B) water molecules and (C) hydrogen atoms on FeNiOOH and RuO_2/FeNiOOH; (D) Optimized water dissociation models on the surfaces of FeNiOOH and RuO_2/FeNiOOH.

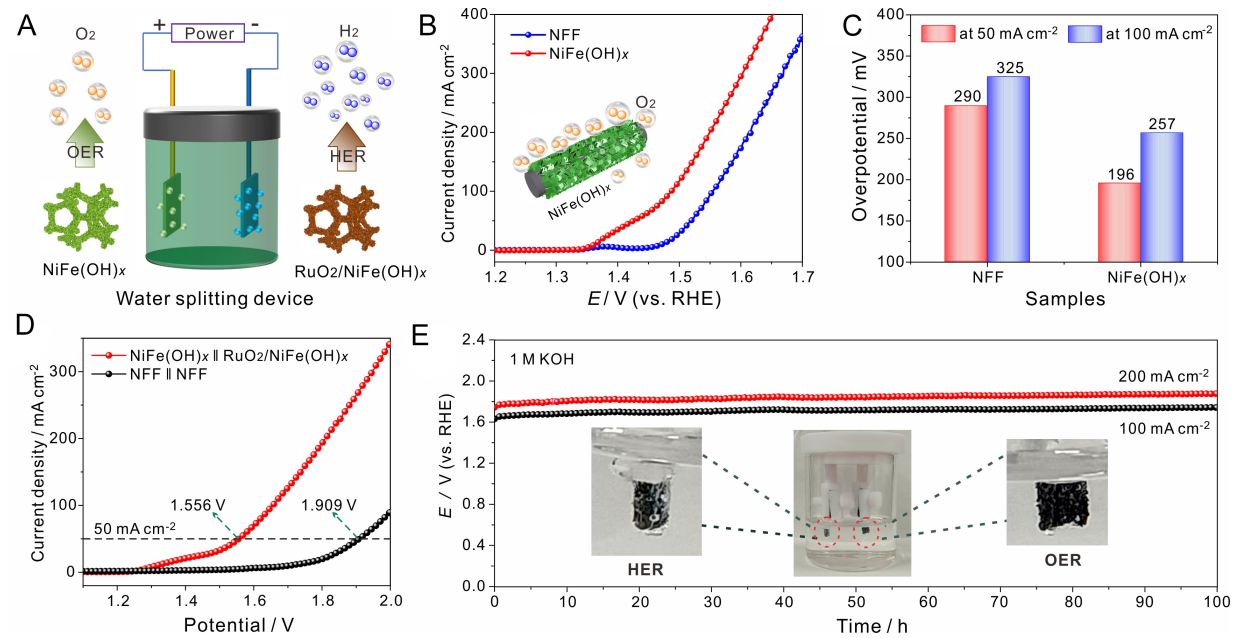

Figure 5. (A) Schematic diagram of the assembled water-splitting electrolyzer; (B) Polarization curves of NFF and $NiFe(OH)_x$ electrodes for OER; (C) A comparative study on the OER overpotentials at the current densities of 50 mA cm^{-2} and 100 mA cm^{-2}; (D) Polarization curves of $NiFe(OH)_x$‖RuO_2/$NiFe(OH)_x$ and NFF‖NFF-based water-splitting devices; (E) Chronopotentiometry curves of the $NiFe(OH)_x$‖RuO_2/$NiFe(OH)_x$ electrolyzer under the constant current densities of 100 mA cm^{-2} and 200 mA cm^{-2} (inset: the photo of water-splitting device operating at 200 mA cm^{-2}). NFF: NiFe foams; HER: hydrogen evolution reaction; OER: oxygen evolution reaction; RHE: reversible hydrogen electrode.

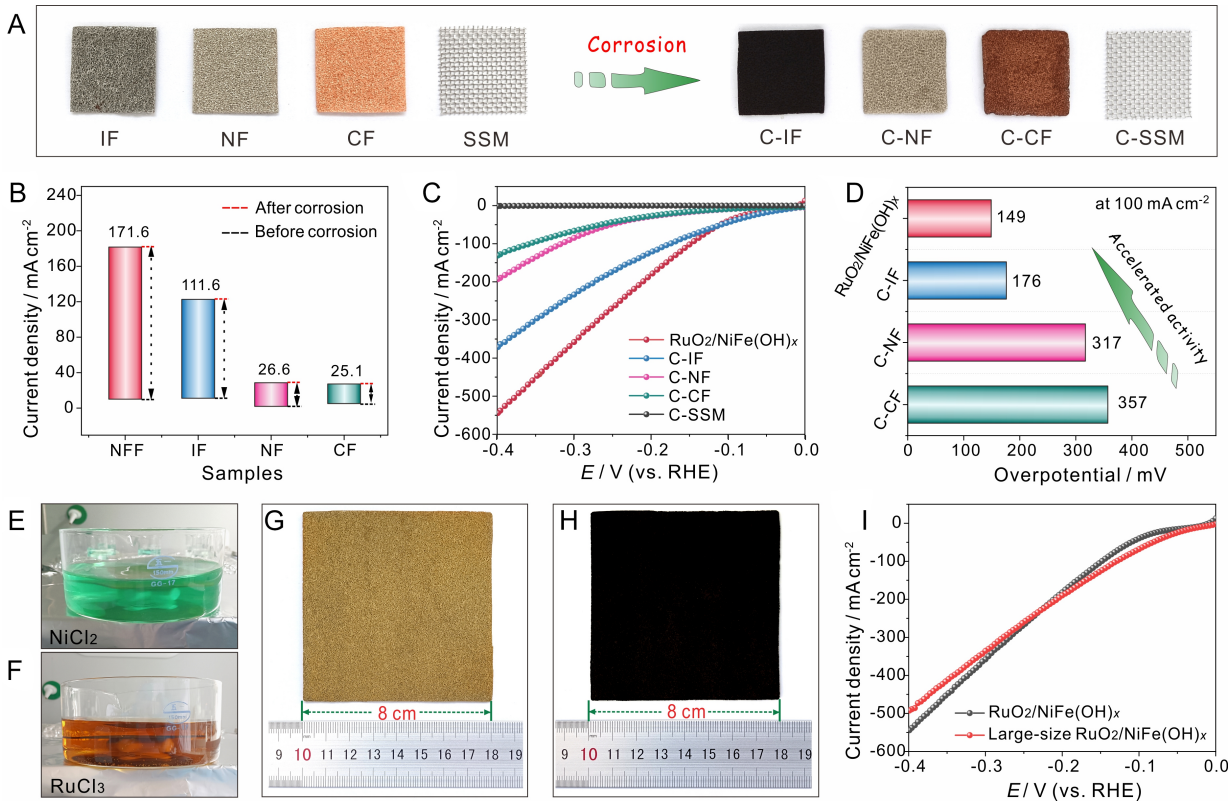

Figure 6. (A) Pictures of the prepared electrodes derived from IF, NF, CF and SSM substrates; (B) A comparison of the current density delivered at 200 mV overpotential; (C) HER polarization curves of the prepared $RuO_2/NiFe(OH)_x$, C-IF, C-NF, C-CF and C-SSM electrocatalysts, and (D) the associated overpotential comparison at 100 mA cm^{-2}; (E and F) Photos of synthesizing large-size $RuO_2/NiFe(OH)_x$ electrode in 100 mM $NiCl_2$ and 2 mM $RuCl_3$ solutions; (G and H) Photos of the prepared large-size $NiFe(OH)_x$ and $RuO_2/NiFe(OH)_x$ electrodes; (I) Polarization curves of $RuO_2/NiFe(OH)_x$ and large-size $RuO_2/NiFe(OH)_x$ for HER. IF: Iron foam; NF: Ni foam; CF: Cu foam; SSM: stainless steel mesh; HER: hydrogen evolution reaction; NFF: NiFe foams; RHE: reversible hydrogen electrode.

To validate the universality of the corrosion-reconstruction strategy, diverse metal substrates, including IF, NF, CF, and SSM, were employed to synthesize HER electrodes, as shown in Figure 6A. Notably, aside from the inherently corrosion-resistant SSM, the colors of the prepared electrodes have all changed, indicative of corrosion reactions taking place. A comparison of the HER polarization curves between pristine substrates and their corrosion-derived electrodes [Supplementary Figure 16] reveals a remarkable enhancement in HER activity for IF, NF, and CF substrates after the corrosion-reconstruction process. Conversely, the HER performance of SSM remained almost unchanged, attributed to its robust corrosion resistance. As evident in Figure 6B and C, a substantial increase in HER current density is observed for the corrosion-derived electrodes. Notably, the $RuO_2/NiFe(OH)_x$ electrode supported on NFF stands out, realizing a remarkable current density of 181.7 mA cm^{-2} at 200 mV, significantly surpassing that of the untreated NFF (10.1 mA cm^{-2}). To attain a current density of 100 mA cm^{-2}, $RuO_2/NiFe(OH)_x$ necessitates a mere overpotential of 149 mV [Figure 6D], underscoring its superior HER electrocatalytic activity in comparison to other electrodes. Furthermore, the corrosion-reconstruction approach is conducted at ambient temperature, facilitating straightforward operation and precise control for achieving the desired scaled-up fabrication. Consequently, we have successfully synthesized the large-sized $NiFe(OH)_x$ and $RuO_2/NiFe(OH)_x$ catalysts (8 × 8 cm^2), as depicted in Figure 6E-H. SEM images shown in Supplementary Figure 17 illustrate that the large-sized $RuO_2/NiFe(OH)_x$ electrode still retains its nanosheet array morphology. The electrode with a 0.25 cm^2 area cut from the 8 * 8 cm^2 electrode was used for testing. The polarization curves presented in Figure 6I indicate that the HER property of the large-size $RuO_2/NiFe(OH)_x$ electrode closely mirrors that of its smaller counterpart (2 × 2 cm^2). More importantly, the long-term durability determination of the bulk electrode demonstrates that it can sustain continuous operation for over 100 h at a large current density of 200 mA cm^{-2} [Supplementary Figure 18]. These comprehensive findings confirm the remarkable universality

of the corrosion-reconstruction strategy in synthesizing high-performance HER electrodes.

CONCLUSIONS

In summary, we engineered RuO_2 nanocluster-endowed NiFe hydroxides [$NiFe(OH)_x$] via a corrosion-reconstruction strategy. Comprehensive characterizations indicate that RuO_2 nanoclusters anchor onto the $NiFe(OH)_x$ surface, forming a highly active reconstructed interface that induces localized electronic rearrangement in the corrosion layers. The resultant RuO_2/$NiFe(OH)_x$ catalyst delivers exceptional HER activity, which only demands 149 mV overpotential to drive the 100 mA cm^{-2} current density. An electrolyzer assembled with this catalyst stably maintains 200 mA cm^{-2} for 100 h. DFT calculations further reveal that RuO_2 introduction reconstructs active sites through electron transfer effects, shifting *H adsorption sites from oxygen to ruthenium atoms. This synergistically optimizes both water dissociation and *H desorption free energy. Moreover, the corrosion-reconstruction strategy demonstrates scalability to large-area electrodes (8 × 8 cm^2) with room-temperature synthesis, highlighting its process simplicity and industrial viability. This work puts forward a promising design approach for efficient non-noble/noble metal hybrid HER catalysts and advances the mechanistic understanding of interfacial electronic modulation in alkaline hydrogen evolution reactions.

DECLARATIONS

Authors' contributions

Chemical syntheses, characterizations and manuscript writing: Mao, C.; Zhang, C.
Data analysis and interpretation: Chen, J.; Cui, Z.
Data curation and technical support: Zhang, R.; Li, X.; Li, R.
Topic selection, manuscript review, editing and supervision: Guo, J.; Liu, Y.; Liu, X.

Availability of data and materials

The data supporting the findings of this study are available within this Article and its Supplementary Materials. Further data are available from the corresponding authors upon request.

AI and AI-assisted tools statement

Not applicable.

Financial support and sponsorship

This work was supported by the National Natural Science Foundation of China (22509054), the Key Research & Development and Promotion Projects in Henan Province (252102241005), the China Postdoctoral Science Foundation (2025M771005), the Postdoctoral Research Grants of Henan Province (HN2025046), and the Key Scientific Research Project of Henan Province Higher Education of China (26A430012).

Conflicts of interest

All authors declared that there are no conflicts of interest.

Ethical approval and consent to participate

Not applicable.

Consent for publication

Not applicable.

Supplementary Materials

Supplementary Materials

REFERENCES

1. Dinh, C.; Jain, A.; de Arquer, F. P. G.; et al. Multi-site electrocatalysts for hydrogen evolution in neutral media by destabilization of water molecules. *Nat. Energy.* **2019**, *4*, 107-14. DOI
2. Wang, P.; Zheng, J.; Li, Y.; et al. Catalyst for industrial-scale seawater electrolysis: inhibit active metal dissolution and chlorine corrosion. *Adv. Sci.* **2025**, *12*, e14301. DOI
3. Zhang, L.; Qi, F.; Ren, R.; et al. Recent advances in green hydrogen production by electrolyzing water with anion-exchange membrane. *Research* **2025**, *8*, 0677. DOI PubMed PMC
4. Kim, M.; Joung, S.; Lee, S.; Kwon, H.; Lee, H. Recent advances in Ni-based electrocatalysts for low-energy hydrogen production via alternative pathways to water electrolysis. *Energy. Mater.* **2025**, *5*, 500097. DOI
5. Guo, F.; Macdonald, T. J.; Sobrido, A. J.; Liu, L.; Feng, J.; He, G. Recent advances in ultralow-Pt-loading electrocatalysts for the efficient hydrogen evolution. *Adv. Sci.* **2023**, *10*, e2301098. DOI
6. Pan, D.; Yu, B.; Tressel, J.; et al. Rapid synthesis of carbon-supported Ru-RuO_2 heterostructures for efficient electrochemical water splitting. *Adv. Sci.* **2025**, *12*, e2414534. DOI
7. Kim, J. H.; Jo, H. J.; Han, S. M.; Kim, Y. J.; Kim, S. Y. Recent advances in electrocatalysts for anion exchange membrane water electrolysis: design strategies and characterization approaches. *Energy. Mater.* **2025**, *5*, 500099. DOI
8. Muthurasu, A.; Natarajan, L.; Kim, T. W.; Ko, T. H.; Lee, Y. J.; Kim, H. Y. Engineering efficient bifunctional electrocatalyst of ruthenium nanocluster heterointerface integrated nickel-iron diselenide for alkaline freshwater and seawater electrolysis. *ACS. Appl. Mater. Interfaces.* **2025**, *17*, 25237-52. DOI PubMed
9. Zhao, Y.; Huang, J.; Zhang, K.; et al. Stable tensile-strained pt single atomic layer catalysts on α-MoC for efficient alkaline hydrogen evolution. *ACS. Nano.* **2025**, *19*, 25273-83. DOI
10. Xiao, J.; Zhang, S.; Sun, Y.; et al. Urchin-like structured MoO_2/Mo_3P/Mo_2C triple-interface heterojunction encapsulated within nitrogen-doped carbon for enhanced hydrogen evolution reaction. *Small* **2023**, *19*, e2206472. DOI
11. He, H.; Mai, J.; Hu, K.; et al. Recent advances in electrocatalysts for efficient hydrogen evolution reaction. *Rare. Metals.* **2025**, *44*, 2208-38. DOI
12. Yu, J.; Zhang, Y.; Zhang, N.; et al. The interface engineering strategy assists the 3D core-shell structure Co_3S_4/CuS@NiFe LDH nanocoral spheres to achieve significant overall water splitting. *Chin. Chem. Lett.* **2026**, *37*, 110830. DOI
13. Liu, B.; Zhong, B.; Li, F.; et al. Co_2P/CoP heterostructures with significantly enhanced performance in electrocatalytic hydrogen evolution reaction: synthesis and electron redistribution mechanism. *Nano. Res.* **2023**, *16*, 12830-9. DOI
14. Xiao, P.; Chen, W.; Wang, X. A review of phosphide-based materials for electrocatalytic hydrogen evolution. *Adv. Energy. Mater.* **2015**, *5*, 1500985. DOI
15. Ren, J. T.; Chen, L.; Tian, W. W.; et al. Rational synthesis of core-shell-structured nickel sulfide-based nanostructures for efficient seawater electrolysis. *Small* **2023**, *19*, e2300194. DOI
16. Guo, Y.; Park, T.; Yi, J. W.; et al. Nanoarchitectonics for transition-metal-sulfide-based electrocatalysts for water splitting. *Adv. Mater.* **2019**, *31*, e1807134. DOI
17. Ma, T.; Cao, H.; Li, S.; et al. Crystalline lattice-confined atomic pt in metal carbides to match electronic structures and hydrogen evolution behaviors of platinum. *Adv. Mater.* **2022**, *34*, e2206368. DOI
18. Tang, S.; Zhang, Z.; Xiang, J.; Yang, X.; Shen, X.; Song, F. Recent advances in transition metal nitrides for hydrogen electrocatalysis in alkaline media: from catalyst design to application. *Front. Chem.* **2022**, *10*, 1073175. DOI PubMed PMC
19. Huang, J.; Wang, J.; Xie, R.; et al. A universal pH range and a highly efficient Mo_2C-based electrocatalyst for the hydrogen evolution reaction. *J. Mater. Chem. A.* **2020**, *8*, 19879-86. DOI
20. Sun, H.; Yao, B.; Han, Y.; et al. Multi-interface engineering of self-supported nickel/yttrium oxide electrode enables kinetically accelerated and ultra-stable alkaline hydrogen evolution at industrial-level current density. *Adv. Energy. Mater.* **2024**, *14*, 2303563. DOI
21. Alsabban, M. M.; Eswaran, M. K.; Peramaiah, K.; et al. Unusual activity of rationally designed cobalt phosphide/oxide heterostructure composite for hydrogen production in alkaline medium. *ACS. Nano.* **2022**, *16*, 3906-16. DOI PubMed PMC
22. Wang, K.; Yan, L.; Mu, X.; et al. One-step hydrothermal synthesis of Mo-doped Ni_3S_2 nanorods for efficient hydrogen evolution reaction. *ACS. Appl. Energy. Mater.* **2022**, *5*, 11498-505. DOI
23. Wang, D.; Pan, Z.; Wu, Z.; Wang, Z.; Liu, Z. Hydrothermal synthesis of MoS_2 nanoflowers as highly efficient hydrogen evolution reaction catalysts. *J. Power. Sources.* **2014**, *264*, 229-34. DOI
24. Liu, X.; Gong, M.; Deng, S.; et al. Transforming damage into benefit: corrosion engineering enabled electrocatalysts for water splitting. *Adv. Funct. Mater.* **2021**, *31*, 2009032. DOI
25. Zhao, Y.; Gao, Y.; Chen, Z.; et al. Trifle Pt coupled with NiFe hydroxide synthesized via corrosion engineering to boost the cleavage of water molecule for alkaline water-splitting. *Appl. Catal. B. Enviro.* **2021**, *297*, 120395. DOI

26. Wu, Z.; Zhao, Y.; Wu, H.; et al. Corrosion engineering on iron foam toward efficiently electrocatalytic overall water splitting powered by sustainable energy. *Adv. Funct. Mater.* **2021**, *31*, 2010437. DOI
27. Lei, L.; Li, F.; Jiang, X.; Yang, H.; Yu Xia, B. Corrosion and protection of electrocatalysts toward advanced energy technologies. *Adv. Funct. Mater.* **2024**, *34*, 2405726. DOI
28. Du, S.; Ren, Z.; Wang, X.; Wu, J.; Meng, H.; Fu, H. Controlled atmosphere corrosion engineering toward inhomogeneous NiFe-LDH for energetic oxygen evolution. *ACS. Nano.* **2022**, *16*, 7794-803. DOI
29. Wan, X.; Song, Y.; Zhou, H.; Shao, M. Layered double hydroxides for oxygen evolution reaction towards efficient hydrogen generation. *Energy. Mater. Adv.* **2022**, *2022*, 2022/9842610. DOI
30. Hao, S.; Chen, L.; Yu, C.; et al. NiCoMo hydroxide nanosheet arrays synthesized via chloride corrosion for overall water splitting. *ACS. Energy. Lett.* **2019**, *4*, 952-9. DOI
31. Li, Z.; Zhang, X.; Zhang, Z.; Chen, P.; Zhang, Y.; Dong, X. Dual-metal hydroxide@oxide heterojunction catalyst constructed via corrosion engineering for large-current oxygen evolution reaction. *Appl. Catal. B. Environ.* **2023**, *325*, 122311. DOI
32. Lin, Z.; Gao, Q.; Lin, C.; Liu, X.; Zhang, Q.; Diao, P. Activating and stabilizing hydrogen evolution on trace-iridium-incorporated nickel hydroxide for energy-efficient hydrogen production. *Appl. Catal. B. Environ. Energy.* **2025**, *378*, 125641. DOI
33. Liu, X.; Wang, X.; Gong, M.; Wang, R.; Hao, X.; Chen, Y. Corrosion strategy for synthesizing Ru-decorated FeOOH nanoneedles as advanced hydrogen evolution reaction catalysts. *J. Alloys. Compd.* **2023**, *958*, 170430. DOI
34. Zhou, Y.; Liu, Y.; Tang, H.; Lin, B. The RuO_2/NiRu heterogeneous interface optimizes the d-band center of the Ni-Ru catalyst for high-performance alkaline hydrogen evolution reaction. *J. Mater. Chem. A.* **2023**, *11*, 10720-6. DOI
35. Nørskov, J. K.; Rossmeisl, J.; Logadottir, A.; et al. Origin of the overpotential for oxygen reduction at a fuel-cell cathode. *J. Phys. Chem. B.* **2004**, *108*, 17886-92. DOI
36. Liu, S.; Li, W.; Ding, H.; et al. Biomineralized RuO_2 nanozyme with multi-enzyme activity for ultrasound-triggered peroxynitrite-boosted ferroptosis. *Small* **2023**, *19*, e2303057. DOI
37. Liu, Y.; Luo, J.; Li, C.; et al. $BaCe_{0.8}Fe_{0.1}Ni_{0.1}O_{3-\delta}$-impregnated Ni-GDC by phase-inversion as an anode of solid oxide fuel cells with on-cell dry methane reforming. *J. Adv. Ceram.* **2024**, *13*, 834-41. DOI
38. Bai, X.; He, W.; Lu, X.; Fu, Y.; Qi, W. Electrochemical oxidation of 5-hydroxymethylfurfural on ternary metal-organic framework nanoarrays: enhancement from electronic structure modulation. *J. Mater. Chem. A.* **2021**, *9*, 14270-5. DOI
39. Chen, S.; Chu, H.; Xie, Z.; et al. Amorphous heterojunction and fluoride-induced effects enable a F-$Ni(OH)_2$/Ni-B electrocatalyst for efficient and stable alkaline freshwater/seawater hydrogen evolution at a high current density. *Inorg. Chem. Front.* **2024**, *11*, 8212-22. DOI
40. Mo, Y.; Du, D.; Du, Y.; Feng, Y.; Tang, P.; Li, D. $Fe(OH)_x$ modified ultra-small Ru nanoparticles for highly efficient hydrogen evolution reaction and its application in water splitting. *J. Colloid. Interface. Sci.* **2024**, *659*, 697-706. DOI
41. Wang, Y.; Liu, Y.; Liu, S.; et al. Gd-induced oxygen vacancy creation activates lattice oxygen oxidation for water electrolysis. *Adv. Funct. Mater.* **2025**, *35*, 2500118. DOI
42. Zhang, T.; Zhao, H. F.; Chen, Z. J.; et al. High-entropy alloy enables multi-path electron synergism and lattice oxygen activation for enhanced oxygen evolution activity. *Nat. Commun.* **2025**, *16*, 3327. DOI PubMed PMC
43. Kwon, N. H.; Kim, M.; Jin, X.; et al. A rational method to kinetically control the rate-determining step to explore efficient electrocatalysts for the oxygen evolution reaction. *NPG. Asia. Mater.* **2018**, *10*, 659-69. DOI